Observation of Quantum Shock Waves Created with Ultra-Compressed Slow Light Pulses in a Bose-Einstein Condensate

Zachary Dutton,[1,2] Michael Budde,[1,3] Christopher Slowe,[1,2] Lene Vestergaard Hau[1,2,3]

We have used an extension of our slow light technique to provide a method for inducing small density defects in a Bose-Einstein condensate. These sub-resolution, micrometer-sized defects evolve into large-amplitude sound waves. We present an experimental observation and theoretical investigation of the resulting breakdown of superfluidity, and we observe directly the decay of the narrow density defects into solitons, the onset of the "snake" instability, and the subsequent nucleation of vortices.

Superfluidity in Bose condensed systems represents conditions where frictionless flow occurs because it is energetically impossible to create excitations. When these conditions are not satisfied, various excitations develop. Experiments on superfluid helium, for example, have provided evidence that the nucleation of vortex rings occurs when ions move through the fluid faster than a critical speed (*1, 2*). Under similar conditions, shock waves would occur in a normal fluid (*3*). Such discontinuities are not allowed in a superfluid, and instead topological defects (such as quantized vortices and solitons) are nucleated when the spatial scale of induced density variations becomes on the order of the healing length. This is the length scale at which the kinetic energy, associated with spatial variations of the macroscopic condensate wave function, becomes on the order of the atom-atom interaction energy (*2, 4*). It is therefore also the minimum length over which the density of a condensate can adjust.

Bose-Einstein condensates (BECs) of alkali atoms (*5*) have provided a system for the study of superfluidity that is theoretically more tractable than liquid helium and allows greater experimental control. An exciting recent development is the production of solitons and vortices. Experiments have used techniques that manipulated the phase of the BEC (*6–9*), or provided the system with a high angular momentum that makes vortex formation energetically favorable (*10, 11*). However, a direct observation of the formation of vortices via the breakdown of superfluidity has been lacking. Rather, rapid heating from "stirring" with a focused laser beam above a critical velocity was observed as indirect evidence of this process (*12, 13*).

In this context, it is natural to ask what would happen if one were to impose a sharp density feature in a BEC with a spatial scale on the order of the healing length. Optical resolution limits have prevented direct creation of this kind of excitation. Here, we present an experimental demonstration of the creation of such defects in sodium Bose-Einstein condensates, using a novel extension of the method of ultraslow light pulse propagation (*14*) via electromagnetically induced transparency (EIT) (*15, 16*).

Our slow light setup is described in (*14*). By illuminating a BEC with a "coupling" laser, we create transparency and low group velocity for a "probe" laser pulse subsequently sent into the cloud. In a geometry where the coupling and probe laser beams propagate at right angles, we can control the propagation of the probe pulse from the side. By introducing a spatial variation of the coupling field along the pulse propagation direction, we vary the group velocity of the probe pulse across the cloud. We accomplish this by blocking half of the coupling beam so that it illuminates only the left side ($z < 0$) of the condensate, setting up a light "roadblock." In this way, we compress the probe pulse to a small spatial region at the center of the BEC while bypassing the usual bandwidth requirements for slow light (*17*). The technique produces a short-wavelength excitation by suddenly removing a narrow disk of the condensate, with the width of the disk determined by the width of the compressed probe pulse.

We find that this excitation results in short-wavelength, large-amplitude sound waves that shed "gray" solitons (*18–20*), in a process analogous to the formation of shock waves in classical fluids. The "snake" (Kadomtsev-Petviashvili) instability is predicted to cause solitons to decay into vortices (*21–24*). This has been observed with optical solitons (*25*), and recently the JILA group predicted and observed that solitons in a BEC decay into vortex rings (*9*). Here, we present a direct observation of the dynamics of the snake instability in a BEC and the subsequent nucleation of vortices. The images of the evolution are compared with numerical propagation of the Gross-Pitaevskii equation in two dimensions.

Details of our Bose-Einstein condensation apparatus can be found in (*26*). We use condensates with about 1.5 million sodium atoms in the state $|1\rangle \equiv |3S_{1/2}, F = 1, M_F = -1\rangle$, where F and M_F are the total spin and spin projection quantum numbers of the atoms, trapped in a 4-Dee magnet [described in (*26*)]. For the experiments presented here, the magnetic trap has an oscillator frequency $\omega_z = (2\pi)21$ Hz along its symmetry direction and a frequency $\omega_x = \omega_y = 3.8\omega_z$ in the transverse directions. The peak density of the condensates is then 9.1×10^{13} cm^{-3}. The temperature is $T \sim 0.5T_c$, where $T_c = 300$ nK is the critical temperature for condensation, and so the vast majority (~90%) of the atoms occupy the ground state.

Creation of the light roadblock. To create slow and spatially localized light pulses, the coupling beam propagates along the x axis (Fig. 1B), is resonant with the D_1 transition from the unoccupied hyperfine state $|2\rangle \equiv |3S_{1/2}, F = 2, M_F = -2\rangle$ to the excited level $|3\rangle \equiv |3P_{1/2}, F = 2, M_F = -2\rangle$, and has a Rabi frequency $\Omega_c = (2\pi)15$ MHz (*27*). We inject probe pulses along the z axis, resonant with the $|1\rangle \rightarrow |3\rangle$ transition and with peak Rabi frequency $\Omega_p = (2\pi)2.5$ MHz. The pulses are Gaussian-shaped with a $1/e$ half-width of $\tau = 1.3$ μs. With the entire BEC illuminated by the coupling beam, we observe probe pulse delays of 4 μs for propagation through the condensates, corresponding to group velocities of 18 m/s at the center of the clouds. A pulse with a temporal half-width τ is spatially compressed from a length $L = 2c\tau$ in vacuum (where c is the speed of light in vacuum) to

$$L = 2\tau V_g = 2\tau \frac{|\Omega_c|^2}{\Gamma f_{13}\sigma_0 n_c} \qquad (1)$$

(*14, 17, 28, 29*) inside the cloud, where V_g is the group velocity of the light pulse in the medium, $\Gamma = (2\pi)10$ MHz is the decay rate of state $|3\rangle$, n_c is the cloud density, $\sigma_0 = 1.65 \times 10^{-9}$ cm^2 is the absorption cross section for light resonant with a two-level atom, and $f_{13} = 1/2$ is the oscillator strength of the $|1\rangle \rightarrow |3\rangle$ transition. The atoms are constantly being driven by the light fields into a dark state, a coherent superposition of the two hyperfine states $|1\rangle$ and $|2\rangle$ (*15*). In the dark state, the ratio of the two population amplitudes is varying in space and time with the electric field amplitude of the probe pulse as

[1]Rowland Institute for Science, 100 Edwin H. Land Boulevard, Cambridge, MA 02142, USA. [2]Lyman Laboratory, Department of Physics, [3]Cruft Laboratory, Division of Engineering and Applied Sciences, Harvard University, Cambridge, MA 02138, USA.

$$\psi_2 = -\frac{\Omega_p}{\Omega_c}\psi_1 \tag{2}$$

where ψ_1, ψ_2 are the macroscopic condensate wave functions associated with the two states $|1\rangle$ and $|2\rangle$.

For the parameters listed above, the probe pulse is spatially compressed from 0.8 km in free space to only 50 μm at the center of the cloud, at which point it is completely contained within the atomic medium. The corresponding peak density of atoms in $|2\rangle$, proportional to $|\psi_2|^2$, is 1/34 of the total atom density. The $|1\rangle$ atoms have a corresponding density depression.

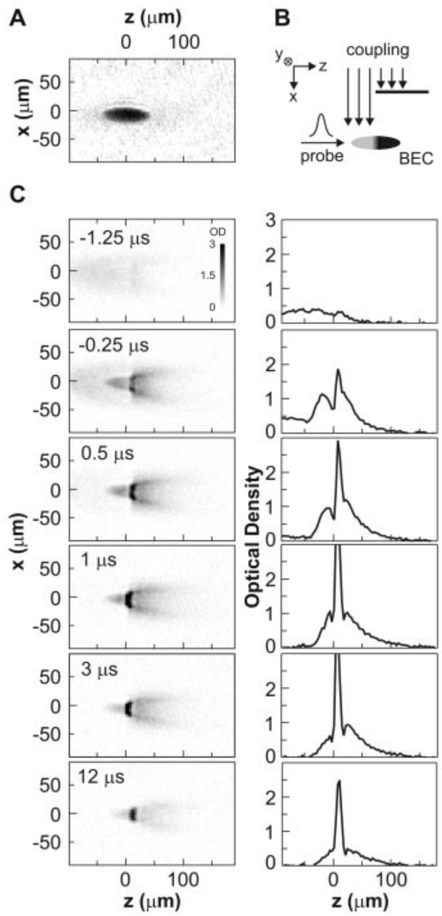

Fig. 1. (**A**) Experimental in-trap OD image of a typical BEC before illumination by the probe pulse and coupling field. The condensate contains 1.5×10^6 atoms. The imaging beam was –30 MHz detuned from the $|1\rangle \rightarrow |3P_{1/2}, F = 2, M_F = -1\rangle$ transition. (**B**) Top view of the beam configuration used to create and study localized defects in a BEC. (**C**) Buildup of state $|2\rangle$ atoms at the roadblock. In-trap OD images (left) show the transfer of atoms from $|1\rangle$ to $|2\rangle$ as the probe pulse propagates through the condensate and runs into the roadblock. The atoms in $|2\rangle$ were imaged with a laser beam –13 MHz detuned from the $|2\rangle \rightarrow |3P_{3/2}, F = 3, M_F = -2\rangle$ transition. To allow imaging, we stopped the probe pulse propagation at the indicated times by switching the coupling beam off (*29*). The time origin $t = 0$ is defined as the moment when the center of the probe pulse enters the BEC from the left. The graphs on the right show the corresponding line cuts along the probe propagation direction through the center of the BEC. The probe pulse had a Rabi frequency $\Omega_p = (2\pi)2.4$ MHz, and the coupling Rabi frequency was $\Omega_c = (2\pi)14.6$ MHz.

From Eqs. 1 and 2, it is clear that to minimize the spatial scale of the density defect, we need to use short pulse widths and low coupling intensities. However, for all the frequency components of the probe pulse to be contained within the transmission window for propagation through the BEC (*17*), we need a pulse with a temporal width τ of at least $2D^{1/2}\Gamma/\Omega_c^2 \approx 0.3$ μs to avoid severe attenuation and distortion ($D \approx 520$ is the column density of a condensate in the z direction times the absorption cross section for on-resonance two-level transitions). Furthermore, we see from Eq. 2 that to maximize the amplitude of the density depression, it would be best to use a peak Rabi frequency for the probe of $\Omega_p \sim \Omega_c$. This also severely distorts the pulse.

Both of these distortion effects accumulate as the pulse propagates through clouds with large D. This motivated us to introduce a roadblock in the condensate for a light pulse approaching from the left side ($z < 0$). By imaging a razor blade onto the right half of the condensate, we ramp the coupling beam from full to zero intensity over the course of a 12-μm region in the middle of the condensate, determined by the optical resolution of the imaging system. In the illuminated region ($z < 0$), our bandwidth and weak-probe requirements are well satisfied and we get undistorted, unattenuated propagation through the first half of the cloud to the high-density, central region of the condensate. As the pulse enters the roadblock region of low coupling intensity, it is slowed down and spatially compressed. The exact shape and size of the defects created with this method are dependent on when absorption effects become important.

Theoretical model. To accurately model the pulse compression and defect formation, we account for the dynamics of the slow light pulses, the coupling field, and the atoms self-consistently. At sufficiently low temperatures, the dynamics of the two-component condensate can be modeled with coupled Gross-Pitaevskii equations (*4, 5*). Here, we include terms to account for the resonant two-photon light coupling between the two components:

$$i\hbar\frac{\partial}{\partial t}\psi_1 = \left[-\frac{\hbar^2\nabla^2}{2m} + V_1(\mathbf{r}) + U_{11}|\psi_1|^2 + U_{12}|\psi_2|^2\right]\psi_1 - i\frac{|\Omega_p|^2}{2\Gamma}\psi_1 - i\frac{\Omega_p{}^*\Omega_c}{2\Gamma}\psi_2 - iN_c\sigma_e\hbar\frac{k_{2\gamma}}{2m}|\psi_2|^2\psi_1$$

$$i\hbar\frac{\partial}{\partial t}\psi_2 = \left[-\frac{\hbar^2(\nabla^2 + i\mathbf{k}_{2\gamma}\cdot\nabla)}{2m} + V_2(\mathbf{r}) + U_{22}|\psi_2|^2 + U_{12}|\psi_1|^2\right]\psi_2 - i\frac{|\Omega_c|^2}{2\Gamma}\psi_2 - i\frac{\Omega_p\Omega_c{}^*}{2\Gamma}\psi_1 - iN_c\sigma_e\hbar\frac{k_{2\gamma}}{2m}|\psi_1|^2\psi_2 \tag{3}$$

where $\hbar$ is the Planck constant divided by 2π, ∇ is the spatial gradient operator, and $V_1(\mathbf{r}) = ½m\omega_z{}^2[\lambda^2(x^2 + y^2) + z^2]$ (where m is the mass of the sodium atoms and $\lambda = 3.8$). Because of the magnetic moment of atoms in state $|2\rangle$, $V_2(\mathbf{r}) = -2V_1(\mathbf{r})$, and atoms in this state are repelled from the trap. The EIT process involves absorption of a probe photon and stimulated emission of a coupling photon, leading to a recoil velocity of 4.1 cm/s for atoms in state $|2\rangle$. This is described by a term in the second part of Eq. 3, containing $\mathbf{k}_{2\gamma} = \mathbf{k}_p - \mathbf{k}_c$, the difference in wave vectors between the two laser beams. (Here, we use a gauge where the recoil momentum is transformed away.) Atom-atom interactions are characterized by the scattering lengths, a_{ij}, via $U_{ij} = 4\pi N_c\hbar^2 a_{ij}/m$, where $a_{11} = 2.75$ nm, $a_{12} = a_{22} = 1.20a_{11}$ (*30*), and N_c is the total number of condensate atoms. To obtain the light coupling terms in Eq. 3, we have adiabatically eliminated the excited-state amplitude ψ_3 (*31*), because the relaxation from spontaneous emission occurs much faster than the light coupling and external atomic dynamics driving ψ_3. In our model, atoms in $|3\rangle$ that spontaneously emit are assumed to be lost from the condensate, which is why the light coupling terms are non-Hermitian. The last term in each equation accounts for losses due to elastic collisions between high-momentum $|2\rangle$ atoms and the nearly stationary $|1\rangle$ atoms ($\sigma_e = 8\pi a_{12}{}^2$) (*32*).

The spatial dynamics of the light fields are described classically with Maxwell's equations in a slowly varying envelope approximation, again using adiabatic elimination of ψ_3:

$$\frac{\partial}{\partial z}\Omega_p = -\frac{1}{2}f_{13}\sigma_0 N_c(\Omega_p|\psi_1|^2 + \Omega_c\psi_1{}^*\psi_2)$$

$$\frac{\partial}{\partial x}\Omega_c = -\frac{1}{2}f_{23}\sigma_0 N_c(\Omega_c|\psi_2|^2 + \Omega_p\psi_1\psi_2{}^*) \tag{4}$$

In the region where the coupling beam is illuminating the BEC ($z < 0$), the light coupling terms dominate the atomic dynamics, and Eqs. 3 and 4 yield Eqs. 1 and 2 above.

We have performed numerical simulations in two dimensions (x and z) to track the behavior of the light fields and the atoms. The probe and coupling fields were propagated according to Eq. 4 with a second-order Runge-Kutta algorithm (*33*) and the atomic mean fields were propagated according to Eq. 3, with an Alternating-Direction Implicit variation of the Crank-Nicolson algorithm (*33, 34*). In this way, Eqs. 3 and 4 were solved self-consistently (*35*). Profiles of the probe pulse intensity along z, through $x = 0$, are shown in Fig. 2A. As the pulse runs into the roadblock, a severe compression of the probe pulse's spatial length occurs. When the probe pulse enters the low coupling region, the Rabi frequency $|\Omega_p|$ becomes on the order of $|\Omega_c|$. Thus, the density of state $|2\rangle$ atoms, $N_c|\psi_2|^2$, increases in a narrow region, which is accompanied by a decrease in $N_c|\psi_1|^2$ (Fig. 2B). The half-width of the defect is 2 μm. As the compression develops, absorption and spontaneous emission events eventually start to remove atoms from the condensate and reduce the probe intensity.

Observation of localized impurity formation in a Bose-Einstein condensate. Experimental results are shown in Fig. 1. Figure 1A is an in-trap image of the original condensate of $|1\rangle$ atoms, Fig. 1B diagrams the beam geometry, and Fig. 1C shows a series of images of state $|2\rangle$ atoms as the pulse propagates into the roadblock. The corresponding optical density (OD) profiles along z through $x = 0$ are also shown. OD is defined to be $-\ln(I/I_0)$ where (I/I_0) is the transmission coefficient of the imaging beam. All imaging is done with near-resonant laser beams propagating along the y axis, and with a duration of 10 μs. There is clearly a buildup of a dense, narrow sample of $|2\rangle$ atoms at the center of the BEC as the pulse propagates to the right. Note that the pulse reaches the roadblock at the top and bottom edges of the cloud before the roadblock is reached at the center, which is a consequence of the transverse variation in the density of the BEC, with the largest density along the center line. After the pulse compression is achieved, we shut off the coupling beam to avoid heating and phase shifts of the atom cloud due to extended exposure to the coupling laser, and we observe the subsequent dynamics of the condensate. (We found that exposure to the coupling laser alone, for the exposure times used to create defects, caused no excitations of the condensates.)

Formation of quantum shock waves. In considering the dynamics resulting from this excitation of a condensate, it should be noted that the roadblock "instantaneously" removes a spatially selected part of ψ_1. The entire light compression happens in ~15 μs. After the pulse is stopped and the coupling laser turned off, the $|2\rangle$ atoms remaining in the condensate ψ_2 have a recoil of 4.1 cm/s, and atoms that have undergone absorption and spontaneous emission events have a similarly sized but randomly directed recoil. Hence, the ψ_2 component and the other recoiling atoms interact with ψ_1 for less than 0.5 ms before leaving the region. Both of these time scales are short relative to the several-millisecond time scale over which most of the subsequent dynamics of ψ_1 occur, as discussed below.

We first considered the one-dimensional (1D) dynamics along the z axis. Snapshots of both condensate components, obtained from numerical propagation in 1D according to Eqs. 3 and 4, are shown in Fig. 3A for various times after the pulse is stopped at the roadblock (and the coupling laser turned off). In the linear hydrodynamic regime, where the density defect has a relative amplitude $A \ll 1$ and a half-width $\delta \gg \xi$ [where $\xi = 1/(8\pi N_c|\psi_1|^2 a_{11})^{1/2}$ is the local healing length, which is 0.4 μm at the center of the ground-state condensate in our experiment], one expects to see two density waves propagating in opposite directions at the local sound speed, $c_s = (U_{11}|\psi_1|^2/m)^{1/2}$, as seen experimentally in (*36*). However, for the parameters used in our experiment, the sound waves are seen to shed sharp features propagating at lower velocities. Examination of the width and speed of these features and the phase jump across them shows that they are gray solitons. With $\psi_1^{(0)}$ describing the slowly varying background wave function of the condensate, the wave function in the vicinity of a gray soliton centered at z_0 is

$$\psi_1(z,t) = \psi_1^{(0)}(z,t)\left\{ i\sqrt{1-\beta^2} + \beta \tanh\left[\frac{\beta}{\sqrt{2}\xi}(z - z_0)\right]\right\} \quad (5)$$

(*18–20*). The dimensionless constant β char-

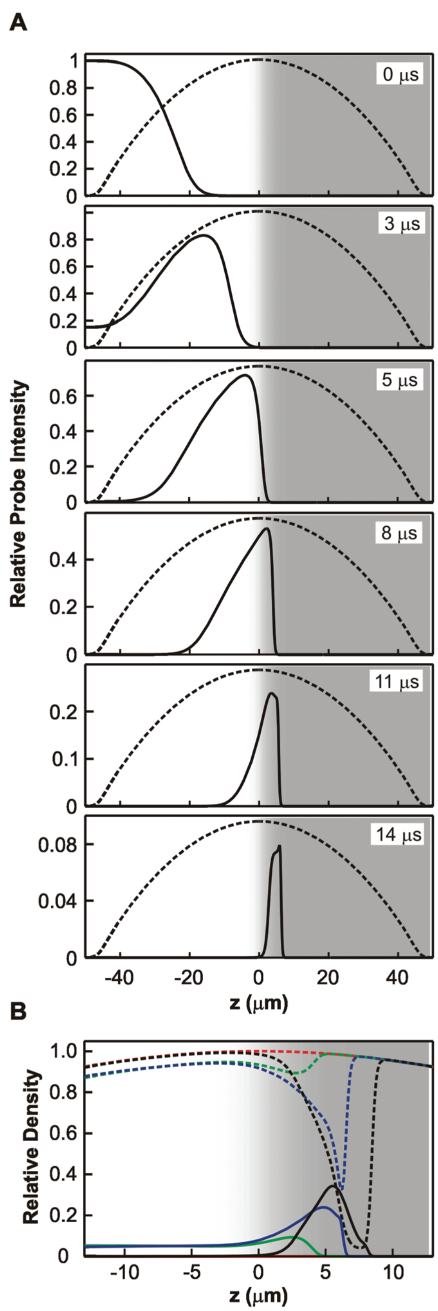

Fig. 2. (**A**) Compression of a probe pulse at the light "roadblock," according to 2D numerical simulations of Eqs. 3 and 4. The solid curves indicate probe intensity profiles along z (at $x = 0$), normalized to the peak input intensity. The snapshots are taken at the indicated times, where $t = 0$ is defined as in Fig. 1C. For reference, the atomic density profile of the original condensate is plotted (in arbitrary units) as a dashed curve. The gray shading indicates the relative coupling input intensity as a function of z, with white corresponding to full intensity and the darkest shade of gray corresponding to zero. The spatial turnoff of the coupling field is centered at $z = 0$ and occurs over 12 μm, as in the experiment. The number of condensate atoms is 1.2×10^6 atoms, the peak density is 6.9×10^{13} cm^{-3}, and the coupling Rabi frequency is $\Omega_c = (2\pi)8.0$ MHz. The probe pulse has a peak Rabi frequency of $\Omega_p = (2\pi)2.5$ MHz and a $1/e$ half-width of $\tau = 1.3$ μs. (**B**) Creation of a narrow density defect in a BEC. Density profiles of the two condensate components, $N_c|\psi_1|^2$ (dashed) and $N_c|\psi_2|^2$ (solid), are shown along z at $x = 0$ for a sequence of times. Note that the z range of the plot is restricted to a narrow region around the roadblock at the cloud center. The densities are normalized relative to the peak density of the original condensate indicated by the red dashed curve. The other curves correspond to times 1 μs (green), 4 μs (blue), and 14 μs (black). The width of the probe pulse is $\tau = 4$ μs and the other parameters are the same as in (A). An animated version is provided in (*40*).

acterizes the "grayness," with $\beta = 1$ corresponding to a stationary soliton with a 100% density depletion. With $\beta \neq 1$, the solitons travel at a fraction of the local sound velocity, $c_s(1 - \beta^2)^{1/2}$. As seen in Fig. 3A, after a shedding event, the remaining part of the sound wave continues to propagate at a reduced amplitude. Our numerical simulations show that the solitons eventually reach a point where their central density is zero and then oscillate back to the other side, in agreement with the discussions in (*18, 20*).

In Fig. 3A, each of the two sound waves sheds two solitons. By considering the available free energy created by a defect, one finds that when the defect size is somewhat larger than the healing length, and the defect amplitude A is on the order of unity, the number of solitons that can be created is approximately $A^{1/2}\delta/(2\xi)$.

One obtains a simple physical estimate of the conditions necessary for soliton shedding by calculating the difference in sound speed associated with the difference in atom density between the center and back edge of the sound wave. As confirmed by our numerical simulations, this difference leads to development of a steeper back edge and an increasingly sharp jump in the phase of the wave function. This is the analog of shock wave formation from large-amplitude sound waves in a classical fluid (*3*). When the spatial width of the back edge has decreased to the width of a soliton with amplitude $\beta = (A/2)^{1/2}$ (according to Eq. 5), such a soliton is shed off the back. Its subsonic speed causes it to separate from the remaining sound wave. Furthermore, by creating defects with sizes on the order of the healing length, we excite collective modes of the condensate, with wave vectors on the order of the inverse healing length. In this regime, the Bogoliubov dispersion relation is not linear (*4, 5*) and, accordingly, some of the sound wave will disperse into smaller ripples, as seen in Fig. 3A.

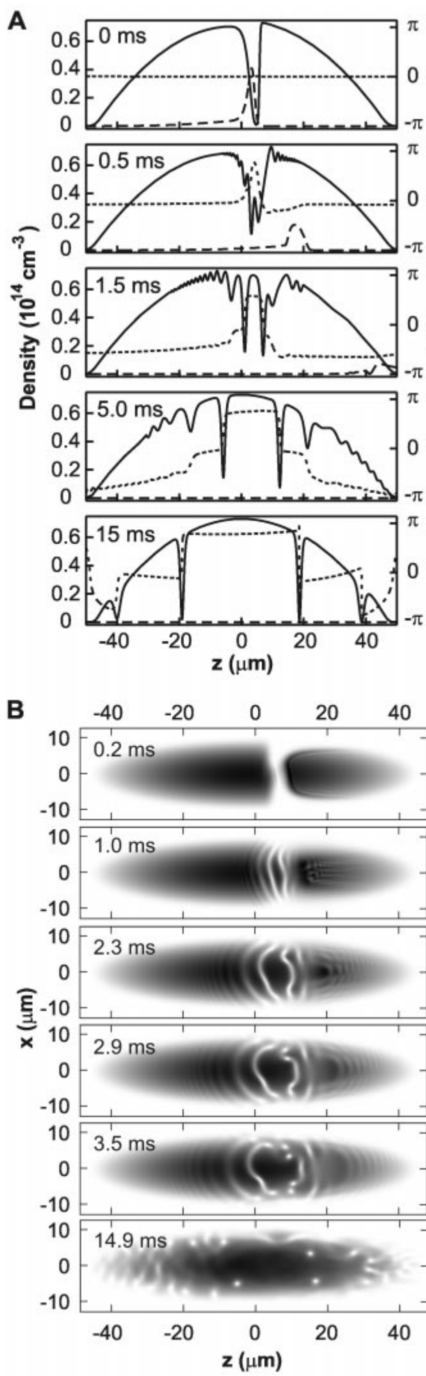

Fig. 3. (**A**) Formation of solitons from a density defect. The plots show results of a 1D numerical simulation of Eqs. 3 and 4. The light roadblock forms a defect, and the subsequent formation of solitons is seen. The defect is set up with the same parameters for the light fields as in Fig. 2B. The number of condensate atoms is $N_c = 1.2 \times 10^6$ and the peak density is 7.5×10^{13} cm^{-3}. The times in the plots indicate the evolution time relative to the time when the probe pulse stops at the roadblock and the coupling beam is switched off (at $t = 8$ μs, with $t = 0$ as defined in Fig. 1C). The solid and dashed curves show the densities of $|1\rangle$ atoms ($N_c|\psi_1|^2$) and $|2\rangle$ atoms ($N_c|\psi_2|^2$). The phase of ψ_1 is shown in each case with a dotted curve (with an arbitrary constant added for graphical clarity). In the first two frames, the $|2\rangle$ atoms quickly leave as a result of the momentum recoil, leaving a large-amplitude, narrow defect in ψ_1 (because this is a 1D simulation, the momentum kick in the x direction is ignored). (**B**) The snake instability and the nucleation of vortices. The plots show the density $N_c|\psi_1|^2$ from a numerical simulation in 2D, with white corresponding to zero density and black to the peak density (6.9×10^{13} cm^{-3}). The parameters are the same as in Fig. 2B, and the times indicated are relative to the coupling beam turnoff at $t = 21$ μs. The solitons curl about their deepest point, eventually breaking and forming vortex pairs of opposite circulation (seen first at 3.5 ms). Several vortices are formed, and the last frame shows the vortices slowly moving toward the edge of the condensate. At later times, they interact with sound waves that have reflected off the condensate boundaries. Animated versions are provided in (*40*).

Considering the evolution of a defect of relative density amplitude A and half-width δ in an otherwise homogeneous medium, we estimate that solitons of amplitude $\beta = (A/2)^{1/2}$ will be created after the two resulting sound waves have propagated a distance

$$z_{\mathrm{sol}} = \frac{2\delta}{A}\left(\frac{1 - \dfrac{\xi}{2\delta}}{1 - \dfrac{\pi^2\xi^2}{\delta^2 A}}\right) \qquad (6)$$

This is in agreement with our numerical calculations. We conclude that the minimum soliton formation length is obtained for large-amplitude defects with a width just a few times the healing length. This dictates the defect width chosen in the experiments presented here. Narrower defects disperse, whereas larger defects, comparable to the cloud size, couple to collective, nonlocalized excitations of the condensate.

Observation of a localized condensate vacancy. We explored the soliton formation experimentally by creating defects in a BEC with the light roadblock. We controlled the size of the defects by varying the intensity of the probe pulses, which had a width $\tau = 1.3$ μs. OD images of state $|1\rangle$ condensates are shown for one particular case in Fig. 4. Immediately after the defect is created, the trap is turned off and the cloud evolves and expands for 1 ms and 10 ms, respectively. As seen from the 1-ms picture, a single deep defect is formed initially, which results in creation of five solitons after 10 ms of condensate dynamics and expansion. The initial defect created in the trap could not be resolved with our imaging system, which has a resolution of 5 μm. By varying the probe intensity, we find a linear relation between the number of solitons formed and the probe pulse energy, as expected.

Dynamics of quantum shock waves. To study the stability of the solitons, we first performed 2D numerical simulations of Eqs. 3 and 4. Figure 3B shows density profiles, $N_c|\psi_1|^2$, obtained for the same parameters as used in Fig. 2B. Again, the profiles are shown at various times after the pulse is compressed and stopped. The deepest soliton (the one closest to the center) is observed to quickly curl and eventually collapse into a vortex pair. The wave function develops a 2π phase shift in a small circle around the vortex cores, which shows that they are singly quantized vortices. Also, the core radius is approximately the healing length. (Upon collapse, a small sound wave between the two vortices carries away some of the remaining soliton energy.) This decay can be understood as resulting from variation in propagation speed along the transverse soliton front. As discussed in (*22–25*), a small deviation will be enhanced by the nonlinearity in the Gross-Pitaevskii equation, and thus the soliton collapses about the deepest (and therefore slowest) point.

Observation of quantum shock waves, snake instability, and nucleation of vortices. Figure 5 shows experimental images of state $|1\rangle$ condensates. After the defect was created, the condensate of $|1\rangle$ atoms was left in the trap for varying amounts of time (as indicated in the figures). The trap was then abruptly turned off and, 15 ms after release, we imaged a selected slice of the expanded condensate (*37*), with a thickness of 30 μm along the *y* direction. The release time of 15 ms was chosen to be large enough that the condensate structures are resolvable with our imaging system (*38*). The slice was optically pumped from state $|1\rangle$ to the $|3S_{1/2}, F = 2\rangle$ manifold for 10 μs before it was imaged with absorption imaging by a laser beam nearly resonant with the transition from $|3S_{1/2}, F = 2\rangle$ to $|3P_{3/2}, F = 3\rangle$. The total pump and imaging time was sufficiently brief that no significant atom motion due to photon recoils occurred during the exposure. The slice was selected at the center of the condensate by placing a slit in the path of the pump beam.

In Fig. 5A, the deepest soliton is seen to curl as it leaves certain sections behind, and at 1.2 ms it has nucleated vortices. This is a direct observation of the snake instability. In Fig. 5B, at 0.5 ms, the snake instability has caused a complicated curving structure in one of the solitons, and vortices are observed after 2.5 ms. The vortices are seen to persist for many milliseconds and slowly drift toward the condensate edge. We observed them even after 30 ms of trap dynamics, long enough to study the interaction of vortices with sound waves reflected off the condensate boundaries. Preliminary results, obtained by varying the *y* position of the imaged condensate slices, indicate a complicated 3D structure of the vortices. In addition, the defect has induced a collective motion of the condensate, whereby atoms originally in the sides of the condensate fill in the defect. This leads to a narrow and dense central region, which then slowly relaxes (Fig. 5B).

We performed the experiment with a variety of Rabi frequencies for the probe pulses, and saw nucleation of vortices only for the peak $\Omega_p > (2\pi)1.4$ MHz. The free energy of a vortex is substantially smaller near the border of the condensate where the density is smaller; thus, smaller (and hence lower energy) defects will form vortices very near the condensate edges, seen as "notches" in Figs. 3B and 5.

Conclusions. We have studied and ob-

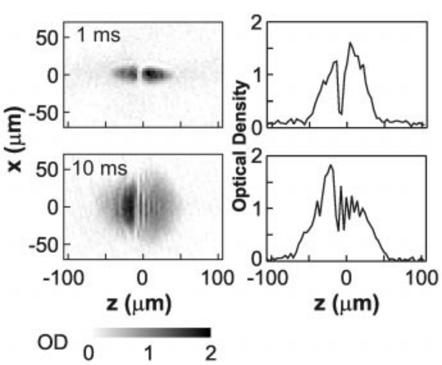

Fig. 4. Experimental OD images and line cuts (at $x = 0$) of a localized defect (top) and the resulting formation of solitons (bottom) in a condensate of $|1\rangle$ atoms. The imaging beam was detuned −30 MHz and −20 MHz, respectively, from the $|3S_{1/2}, F = 2\rangle \rightarrow |3P_{3/2}, F = 3\rangle$ transition. Before imaging, the atoms were optically pumped to $|3S_{1/2}, F = 2\rangle$ for 10 μs. The probe pulse had a peak Rabi frequency $\Omega_p = (2\pi)2.4$ MHz. The coupling laser had a Rabi frequency $\Omega_c = (2\pi)14.9$ MHz, was turned on 6 μs before the probe pulse maximum, and had a duration of 18 μs.

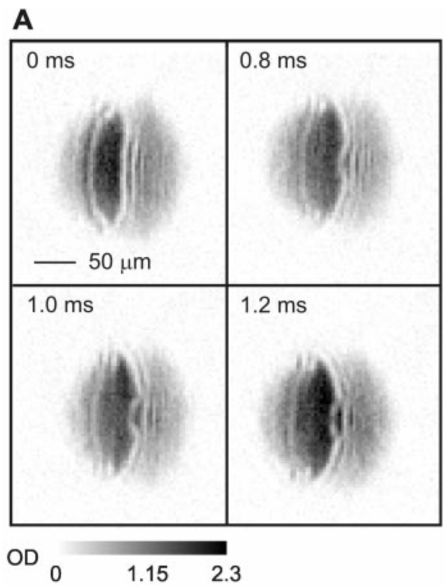

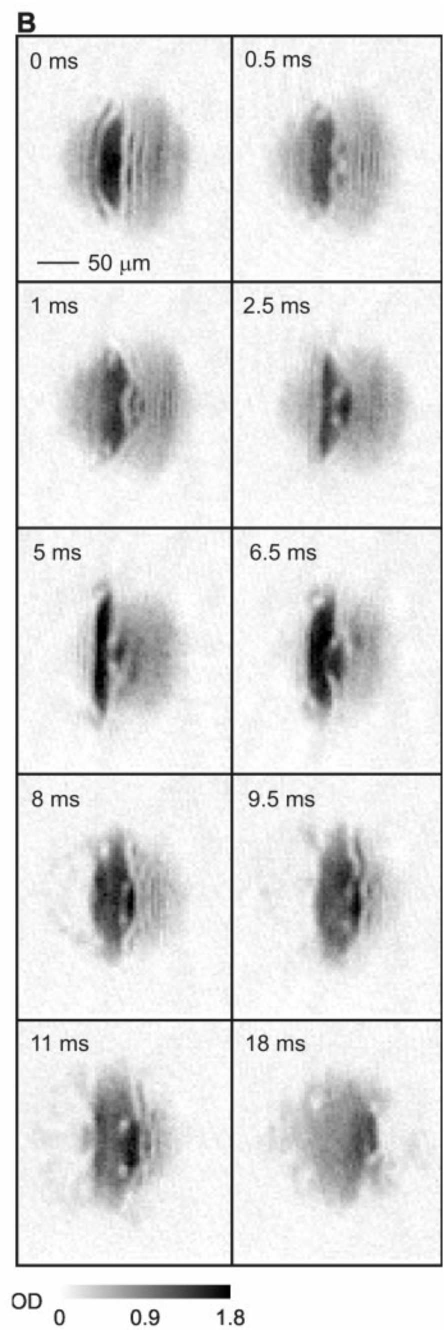

Fig. 5. Experimental OD images of a $|1\rangle$ condensate, showing development of the snake instability and the nucleation of vortices. In each case, the BEC was allowed to evolve in the trap for a variable amount of time after defect creation. (**A**) The deepest soliton (nearest the condensate center) curls as a result of the snake instability and eventually breaks, nucleating vortices at 1.2 ms. Defects were produced in BECs with 1.9×10^6 atoms by probe pulses with a peak $\Omega_p = (2\pi)2.4$ MHz and a coupling laser with $\Omega_c = (2\pi)14.6$ MHz. The imaging beam was −5 MHz detuned from the $|3S_{1/2}, F = 2\rangle \rightarrow |3P_{3/2}, F = 3\rangle$ transition. (**B**) The snake instability and behavior of vortices at later times. The parameters in this series are the same as in (A), except that the peak $\Omega_p = (2\pi)2.0$ MHz, the number of atoms in the BECs was 1.4×10^6, and the pictures were taken with the imaging beam on resonance.

served how short-wavelength excitations cause a breakdown of superfluidity in a BEC. Our results show how localized defects in a superfluid will quite generally either disperse into high-frequency ripples or end up in the form of topological defects such as solitons and vortices, and we have obtained an analytic expression for the transition between the two regimes. By varying our experimental parameters, we can create differently sized and shaped defects and can also control the number of defects created, allowing studies of a myriad of effects. Among them are soliton-soliton collisions, more extensive studies of soliton stability, soliton–sound wave collisions, vortex-soliton interactions, vortex dynamics, interaction between vortices, and the interaction between the BEC collective motion and vortices.

References and Notes

1. R. J. Donnelly, *Quantized Vortices in Helium II* (Cambridge Univ. Press, Cambridge, 1991).
2. R. M. Bowley, *J. Low Temp. Phys.* **87**, 137 (1992).
3. L. D. Landau, E. M. Lifshitz, *Fluid Mechanics* (Pergamon, New York, 1959).
4. A. L. Fetter, in *Bose-Einstein Condensation in Atomic Gases, Proceedings of the International School of Physics Enrico Fermi, Course CXL,* M. Inguscio, S. Stringari, C. Wieman, Eds. (International Organisations Services, Amsterdam, 1999), pp. 201–263.
5. For a review, see F. Dalfovo, S. Giorgini, L. P. Pitaevskii, S. Stringari, *Rev. Mod. Phys.* **71**, 463 (1999).
6. M. R. Matthews *et al.*, *Phys. Rev. Lett.* **83**, 2498 (1999).
7. S. Burger, K. Bongs, S. Dettmer, W. Ertmer, K. Sengstock, *Phys. Rev. Lett.* **83**, 5198 (1999).
8. J. Denschlag *et al.*, *Science* **287**, 97 (2000).
9. B. P. Anderson *et al.*, *Phys. Rev. Lett.* **86**, 2926 (2001).
10. K. W. Madison, F. Chevy, W. Wohlleben, J. Dalibard, *Phys. Rev. Lett.* **84**, 806 (2000).
11. J. R. Abo-Shaeer, C. Raman, J. M. Vogels, W. Ketterle, *Science* **292**, 476 (2001).
12. C. Raman *et al.*, *Phys. Rev. Lett.* **83**, 2502 (1999).
13. B. Jackson, J. F. McCann, C. S. Adams, *Phys. Rev. A* **61**, 051603(R) (2000).
14. L. V. Hau, S. E. Harris, Z. Dutton, C. H. Behroozi, *Nature* **397**, 594 (1999).
15. S. E. Harris, *Phys. Today* **50**, 36 (1997).
16. M. O. Scully, M. S. Zubairy, *Quantum Optics* (Cambridge Univ. Press, Cambridge, 1997).
17. S. E. Harris, L.V. Hau, *Phys. Rev. Lett.* **82**, 4611 (1999).
18. S. A. Morgan, R. J. Ballagh, K. Burnett, *Phys. Rev. A* **55**, 4338 (1997).
19. W. P. Reinhardt, C. W. Clark, *J. Phys. B* **30**, L785 (1997).
20. Th. Busch, J. R. Anglin, *Phys. Rev. Lett.* **84**, 2298 (2000).
21. B. B. Kadomtsev, V. I. Petviashvili, *Sov. Phys. Dokl.* **15**, 539 (1970).
22. C. A. Jones, S. J. Putterman, P. H. Roberts, *J. Phys. A* **19**, 2991 (1986).
23. C. Josserand, Y. Pomeau, *Europhys. Lett.* **30**, 43 (1995).
24. D. L. Feder, M. S. Pindzola, L. A. Collins, B. I. Schneider, C. W. Clark, *Phys. Rev. A* **62**, 053606 (2000).
25. A. V. Mamaev, M. Saffman, A. A. Zozulya, *Phys. Rev. Lett.* **76**, 2262 (1996).
26. L. V. Hau *et al.*, *Phys. Rev. A* **58**, R54 (1998).
27. We use the definition $\Omega_p = \mathbf{E}_{p0} \cdot \mathbf{d}_{13}$, $\Omega_c = \mathbf{E}_{c0} \cdot \mathbf{d}_{23}$, where $\mathbf{E}_{p0}$, $\mathbf{E}_{c0}$ are the slowly varying electric field amplitudes, and $\mathbf{d}_{13}$, $\mathbf{d}_{23}$ are the electric dipole matrix elements of the transitions.
28. S. E. Harris, J. E. Field, A. Kasapi, *Phys. Rev. A* **46**, R29 (1992).
29. C. Liu, Z. Dutton, C. H. Behroozi, L. V. Hau, *Nature* **409**, 490 (2001).
30. J. P. Burke, C. H. Greene, J. L Bohn, *Phys. Rev. Lett.* **81**, 3355 (1998). A Mathematica notebook is available at http://fermion.colorado.edu/~chg/Collisions.
31. J. Javanainen, J. Ruostekoski, *Phys. Rev. A* **52** 3033 (1995).
32. Y. B. Band, M. Tribbenbach, J. P. Burke, P. S. Julienne, *Phys. Rev. Lett.* **84**, 5462 (2000).
33. W. H. Press, S. A. Teukolsky, W. T. Vetterling, B. P. Flannery, *Numerical Recipes in C* (Cambridge Univ. Press, Cambridge, ed. 2, 1992).
34. S. E. Koonin, D. C. Merideth, *Computational Physics* (Addison-Wesley, Reading, MA, 1990).
35. For propagation of the Gross-Pitaevskii equation in 1D, we typically used a spatial grid with 4000 points and $dz = 0.040$ μm. In 2D simulations, we typically used a 750×750 grid with $dz = 0.21$ μm and $dx = 0.057$ μm. To solve the equations self-consistently, we kept track of the wave functions at previous time points and projected forward to second order. Smaller time steps and grid spacing were also used to assure convergence of the results. To mimic the nonlinear interaction strength at the center of a 3D cloud, we put in an effective condensate radius [calculated with the Thomas-Fermi approximation (*39*)] in the dimensions that were not treated dynamically. In all calculations, the initial condition was the ground-state condensate wave function with all atoms in $|1\rangle$, obtained by propagating a Thomas-Fermi wave function in imaginary time.
36. M. R. Andrews *et al.*, *Phys. Rev. Lett.* **79**, 553 (1997).
37. M. R. Andrews *et al.*, *Science* **275**, 637 (1997).
38. F. Dalfavo, M. Modugno, *Phys. Rev. A* **61**, 023605 (2000).
39. G. Baym, C. Pethick, *Phys. Rev. Lett.* **76**, 6 (1996).
40. Supplementary material is available at *Science* Online (www.sciencemag.org/cgi/content/full/1062527/DC1).

41. Supported by a National Defense Science and Engineering Grant sponsored by the U.S. Department of Defense (C.S.), the Rowland Institute for Science, the Defense Advanced Research Projects Agency, the U.S. Air Force Office of Scientific Research, the U.S. Army Research Office OSD Multidisciplinary University Research Initiative Program, the Harvard Materials Research Science and Engineering Center (sponsored by NSF), and the Carlsberg Foundation, Denmark.

15 May 2001; accepted 11 June 2001
Published online 28 June 2001;
10.1126/science.1062527
Include this information when citing this paper.

The Composite Genome of the Legume Symbiont *Sinorhizobium meliloti*

Francis Galibert,[1] Turlough M. Finan,[2] Sharon R. Long,[3,4,*] Alfred Pühler,[5] Pia Abola,[6] Frédéric Ampe,[7] Frédérique Barloy-Hubler,[1] Melanie J. Barnett,[3] Anke Becker,[5] Pierre Boistard,[7] Gordana Bothe,[8] Marc Boutry,[9] Leah Bowser,[6] Jens Buhrmester,[5] Edouard Cadieu,[1] Delphine Capela,[1,7,†] Patrick Chain,[2] Alison Cowie,[2] Ronald W. Davis,[6] Stéphane Dréano,[1] Nancy A. Federspiel,[6,‡] Robert F. Fisher,[3] Stéphanie Gloux,[1] Thérèse Godrie,[10] André Goffeau,[9] Brian Golding,[2] Jérôme Gouzy,[7] Mani Gurjal,[6] Ismael Hernandez-Lucas,[2] Andrea Hong,[3] Lucas Huizar,[6] Richard W. Hyman,[6] Ted Jones,[6] Daniel Kahn,[7] Michael L. Kahn,[11] Sue Kalman,[6,§] David H. Keating,[3,4] Ernö Kiss,[7] Caridad Komp,[6] Valérie Lelaure,[1] David Masuy,[9] Curtis Palm,[6] Melicent C. Peck,[3] Thomas M Pohl,[8] Daniel Portetelle,[10] Bénédicte Purnelle,[9] Uwe Ramsperger,[8] Raymond Surzycki,[6,‖] Patricia Thébault,[7] Micheline Vandenbol,[10] Frank-J. Vorhölter,[5] Stefan Weidner,[5] Derek H. Wells,[3] Kim Wong,[2] Kuo-Chen Yeh,[3,4,¶] Jacques Batut[7]

The scarcity of usable nitrogen frequently limits plant growth. A tight metabolic association with rhizobial bacteria allows legumes to obtain nitrogen compounds by bacterial reduction of dinitrogen (N_2) to ammonium (NH_4^+). We present here the annotated DNA sequence of the α-proteobacterium *Sinorhizobium meliloti*, the symbiont of alfalfa. The tripartite 6.7-megabase (Mb) genome comprises a 3.65-Mb chromosome, and 1.35-Mb pSymA and 1.68-Mb pSymB megaplasmids. Genome sequence analysis indicates that all three elements contribute, in varying degrees, to symbiosis and reveals how this genome may have emerged during evolution. The genome sequence will be useful in understanding the dynamics of interkingdom associations and of life in soil environments.

Symbiotic nitrogen fixation is profoundly important for the environment. Most plants assimilate mineral nitrogen only from soil or added fertilizer. An alternative source powered by photosynthesis, rhizobia-legume symbioses provide a major source of fixed